

# III-V-on-silicon solar cells reaching 33% photoconversion efficiency in two-terminal configuration

Romain Cariou<sup>1,4\*</sup>, Jan Benick<sup>1</sup>, Frank Feldmann<sup>1,2</sup>, Oliver Höhn<sup>1</sup>, Hubert Hauser<sup>1</sup>, Paul Beutel<sup>1</sup>, Nasser Razek<sup>3</sup>, Markus Wimplinger<sup>3</sup>, Benedikt Bläsi<sup>1</sup>, David Lackner<sup>1</sup>, Martin Hermle<sup>1</sup>, Gerald Siefer<sup>1</sup>, Stefan W. Glunz<sup>1,2</sup>, Andreas W. Bett<sup>1</sup> and Frank Dimroth<sup>1</sup>

**Silicon dominates the photovoltaic industry but the conversion efficiency of silicon single-junction solar cells is intrinsically constrained to 29.4%, and practically limited to around 27%. It is possible to overcome this limit by combining silicon with high-bandgap materials, such as III-V semiconductors, in a multi-junction device. Significant challenges associated with this material combination have hindered the development of highly efficient III-V/Si solar cells. Here, we demonstrate a III-V/Si cell reaching similar performances to standard III-V/Ge triple-junction solar cells. This device is fabricated using wafer bonding to permanently join a GaInP/GaAs top cell with a silicon bottom cell. The key issues of III-V/Si interface recombination and silicon's weak absorption are addressed using poly-silicon/SiO<sub>x</sub> passivating contacts and a novel rear-side diffraction grating for the silicon bottom cell. With these combined features, we demonstrate a two-terminal GaInP/GaAs//Si solar cell reaching a 1-sun AM1.5G conversion efficiency of 33.3%.**

Crystalline silicon solar cells have been dominating the photovoltaic market for decades. Today, the overall cost of photovoltaics is driven by system components such as installation, cabling and inverters. Since most of these costs are area-dependent, for a further reduction of the levelized cost of electricity, it is crucial to improve the conversion efficiency. State-of-the-art industrial crystalline silicon solar cells have conversion efficiencies in the range of 20–21% while a few laboratory-type champion devices reach more than 25%<sup>1–9</sup>, with 26.7%<sup>10</sup> being the current record efficiency. The theoretical Shockley–Queisser radiative efficiency limit<sup>11</sup> for silicon solar cells with a bandgap of 1.12 eV is 33%. However, due to silicon's indirect bandgap, Auger recombination becomes the dominant intrinsic loss channel, which reduces the theoretical upper limit to 29.4%<sup>12</sup>. Realistic boundary conditions such as the necessity to attach contacts to the cell and incomplete light harvesting reduce the practical efficiency limit to around 27%<sup>3</sup>. Thus, pure crystalline silicon solar cells are extremely close to their performance limit; new concepts are becoming crucial.

A well-known strategy for increasing solar cell conversion efficiency is the multi-junction architecture in which a set of semiconductor absorbers with appropriate bandgaps are used. This approach reduces thermalization losses arising from the absorption of photons with excess energy compared to the semiconductor bandgap, as well as transmission losses of photons with insufficient energy. Various multi-junction approaches are found in the literature. First, solar cells can be integrated in an optical system, splitting the light into different wavelength bands that are then redirected onto solar cells with appropriate bandgaps<sup>13–16</sup>. Alternatively, individual solar cells can be mechanically stacked with separate contacts on each cell, referred to as the multi-terminal approach<sup>17,18</sup>. By doing so, no subcell current matching is required if every cell has its own electric

circuit throughout the photovoltaic module and its own inverter. An efficiency of 35.9% was recently reported for a mechanically stacked four-terminal device (GaInP/GaAs on silicon, 1 cm<sup>2</sup>, AM1.5G); by connecting all subcells in series, this device reaches 30.9% efficiency<sup>19</sup>.

However, all industrially scaled multi-junction cell architectures so far (space application, concentrating photovoltaics or thin-film cells) use a two-terminal approach. This is due to the lower complexity of producing these devices and implementing them into photovoltaic modules. Two-terminal cells can be connected by standard series or parallel connection with little space between the cells and with only one electric circuit. Moreover, the parasitic absorption in non-photoactive layers is reduced (no intermediate electrodes in the device). Thus, it is expected that two-terminal cells will also be favourable for future applications of high-performance III-V-on-silicon (III-V//Si; the double slash symbol refers to monolithic two-terminal integration hereafter) tandem solar cells. However, it should be mentioned that micro-inverters with high reliability and low cost may enable new architectures for multi-terminal devices in the future. Two material systems are currently discussed as high-bandgap absorbers on silicon: perovskites<sup>20–22</sup> and III-V materials<sup>23–26</sup>. While the first approach has a clear low-cost potential, its stability and reproducibility are still major issues. In contrast, III-V photovoltaics, while being more expensive, are a proven high-efficiency technology, already used in space satellites and concentrating photovoltaics, with champion cell efficiencies up to 38.8% for a five-junction solar cell measured at 1 sun and 46% for a four-junction device measured at 508 suns<sup>10</sup>. Experimentally, III-V solar cells achieve the highest spectral efficiency among the high-bandgap materials and thus appear as ideal tandem partners for silicon, efficiency-wise<sup>27</sup>. To apply III-V on silicon, strategies to

<sup>1</sup>Fraunhofer Institute for Solar Energy Systems ISE, Freiburg, Germany. <sup>2</sup>Laboratory for Photovoltaic Energy Conversion, University of Freiburg, Freiburg, Germany. <sup>3</sup>EV Group E. Thallner GmbH, St Florian am Inn, Austria. <sup>4</sup>Present address: Université Grenoble Alpes, CEA, LITEN, INES, Grenoble, France. \*e-mail: [romain.cariou@cea.fr](mailto:romain.cariou@cea.fr)

grow epitaxial III–V layers directly on silicon have been investigated by generations of scientists<sup>28</sup>. However, best-in-class direct-grown III–V//Si solar cells resulting from this approach are still limited to ~20% efficiency<sup>29,30</sup>. Indeed, the different lattice constant and thermal expansion coefficient, but also the combination of polar and nonpolar materials and the high sensitivity of silicon to low levels of impurities, remain significant challenges<sup>31</sup> that require further research and development.

In this work, we choose a different approach inspired by the microelectronics sector: surface-activated wafer bonding. While being difficult to scale to high-throughput gigawatt manufacturing, this technique bypasses many of the above-mentioned constraints. We use surface-activated wafer bonding to join an independently prepared silicon bottom cell with a GaInP/GaAs top cell, thus forming a monolithic two-terminal device with three series-connected p–n junctions<sup>26</sup>. For the silicon bottom cell, we use an advanced architecture with two innovative features. The first feature is silicon passivating contacts<sup>32,33</sup> to enhance the open-circuit voltage of the silicon bottom cell. The second feature is a diffraction grating to enhance the internal light trapping of the indirect-bandgap semiconductor silicon. The doped poly-silicon/ultrathin SiO<sub>x</sub> contact stack provides an excellent surface passivation for planar surfaces, which prevents recombination at the III–V//Si interface and remains unaltered during the III–V top-cell processing. Applying a rear-side diffraction grating enables an infrared-optimized design while preserving flat surfaces for the silicon cell<sup>34,35</sup>. Thus, the silicon cell is still fully compatible with the wafer bonding process and the surface area is not enlarged, which would increase effective surface recombination. With this electrically flat and optically structured bottom silicon cell design, we demonstrate a two-terminal 4 cm<sup>2</sup> III–V//Si triple-junction solar cell reaching a 1-sun AM1.5G efficiency of 33.3%.

### III–V//Si solar cell design

The layer stack and band structure of the Ga<sub>0.51</sub>In<sub>0.49</sub>P/GaAs//Si solar cell fabricated in this study are shown in Fig. 1a,b, while a picture of the final device with bright red electroluminescence (EL) from the GaInP top cell is displayed in Fig. 1c. Both Ga<sub>0.51</sub>In<sub>0.49</sub>P and GaAs are direct semiconductors with the lowest transition energy at the  $\Gamma$  point. This leads to high absorption and allows the III–V layers to have a total thickness of only 1.9  $\mu$ m.

Photons that are transmitted through the GaAs reach the silicon bottom cell. We use here an advanced p-type silicon solar cell, featuring passivating contacts based on doped poly-silicon layers (90 nm thick) with ultrathin (~1.2 nm) SiO<sub>x</sub> on both sides<sup>32,33</sup>. This architecture, inspired by bipolar junction transistors, was early identified as a promising approach for solar cells<sup>36,37</sup>. Indeed, the stack of ultrathin full-area interfacial oxides with a doped poly-silicon layer suppresses the recombination of minority carriers while permitting majority carrier extraction from the silicon wafer<sup>32,38,39</sup>. Due to the fact that silicon is an indirect semiconductor (lowest transition energy at the X point), the absorption of photons near the band edge is significantly lower compared to the III–V top cells. However, as described further in this paper, the optical light path, and thus absorption of long-wavelength photons ( $\geq 1,000$  nm), can be effectively increased by applying back-side diffraction structures on top of the bottom passivating hole contact. Details about the cell fabrication processes are reported in the Methods.

### III–V//Si bond interface microstructure

A key point of our approach is the direct crystal connection between the III–V top cells and the silicon bottom cell. Fabricating a high-performance device in the two-terminal configuration requires a mechanically stable and optically transparent low-resistance path for majority carriers at the III–V//Si interface. As shown in Fig. 1a, we connect an n-GaAs  $1 \times 10^{19}$  atoms cm<sup>-3</sup> layer directly to the poly-

Si bottom cell emitter, with a doping level of  $1 \times 10^{20}$  atoms cm<sup>-3</sup>, by means of direct semiconductor bonding<sup>40</sup> (see Methods for process details). Figure 2a–c shows schematics of the device; a low-magnification GaInP/GaAs//Si cross-section scanning transmission electron microscope high-angle annular dark-field image (STEM-HAADF), and a high-resolution transmission electron microscope zoom of the cross-section of the GaAs//poly-Si interface are displayed. At the micrometre scale, a sharp III–V//Si interface is visible, but the nanometre scale reveals, nonetheless, a ~1–2-nm-thick amorphous interlayer, which results from the surface sputtering before bonding<sup>41</sup>. This interlayer enables the transition between the silicon and GaAs crystalline lattices (mismatch of 4%) and obviates the formation of misfit/threading dislocations that would alter the device performance. Figure 2d–f shows a STEM-HAADF zoom of the interface and the corresponding STEM energy-dispersive X-ray spectroscopy (STEM-EDXS) silicon and oxygen maps of the area. The ultrathin tunnel SiO<sub>x</sub> appears clearly at the c-Si/poly-Si interface, as well as some remaining oxide from the cleaning procedure at the GaAs//poly-Si interface. A similar interface was reported in the case of GaAs//c-Si bonds, which was found to be transparent for photons below the GaAs bandgap and with a low interface resistance<sup>26</sup> of only a few milliohms per square centimetre. Additional STEM-HAADF and STEM-EDXS maps of In, As, P, Al, Ga and Si elements measured on GaInP/GaAs//Si solar cell cross-sections are shown in Supplementary Fig. 1.

### NaNPlanar III–V//Si two-terminal solar cell performance

A picture of the final solar cell wafer is shown in Fig. 3a: our design features twelve 4 cm<sup>2</sup> cells and four 1 cm<sup>2</sup> cells, separated by etched trenches (6  $\mu$ m into the silicon wafer). The double-layer anti-reflection coating results in the general dark appearance of the cells. The distribution of open-circuit voltage ( $V_{oc}$ ), fill factor (FF) and short-circuit current density ( $J_{sc}$ ), summarized in Fig. 3c–e, has a relatively small spread with a limited number of outliers. The  $V_{oc}$  map, normalized to the best cell voltage (see Fig. 3b), demonstrates the good performance homogeneity. Interestingly, cells with de-bonded areas suffer from strong series resistance but still have high  $V_{oc}$  owing to the effective passivation of the silicon cell. The best cell of the wafer, highlighted on the picture, was measured at Fraunhofer ISE CaLab. Figure 3f shows the device's external quantum efficiency (EQE), which reaches between 90 and 95% in the 470–1,010 nm wavelength range, for a weighted reflection of 2.3% (front metal grid included). From top to bottom, the photo-generated current densities for each junction calculated with the AM1.5G spectrum are 12.7 mA cm<sup>-2</sup>, 13.1 mA cm<sup>-2</sup> and 11.6 mA cm<sup>-2</sup>. While the GaInP/GaAs top cells are relatively close to current matching, the planar silicon cell, with weak near-infrared absorption, limits the whole series-connected device. The calibrated current–voltage ( $I$ – $V$ ) curve and cell parameters are displayed in Fig. 3g. With a FF of 0.865 and a  $V_{oc}$  of 3.125 V, the cell reaches 31.4% efficiency. With additional EL measurements (see Methods and Supplementary Figs. 2 and 3), we could extract the voltages of the individual subcells: 1.412 V, 1.024 V and 0.692 V from top to bottom. Thus, using the silicon passivating contact approach allows a significant  $V_{oc}$  gain of 65 mV compared to a silicon bottom cell with a non-passivated phosphorus-doped emitter<sup>26</sup>. This high voltage demonstrates that the passivating contact architecture is extremely relevant for silicon-based multi-junctions. However, for this current design, optical simulations clearly reveal that the short-circuit current density is limited by the poor light trapping in the double-side polished silicon bottom solar cell. Thus, light-trapping structures are clearly needed to enhance near-bandgap absorption.

### Boosting Si infrared response with photonic light trapping

High-efficiency silicon solar cells commonly use light-trapping features, such as random pyramids on the front (and sometimes rear) side, to compensate for the weak near-bandgap absorption.

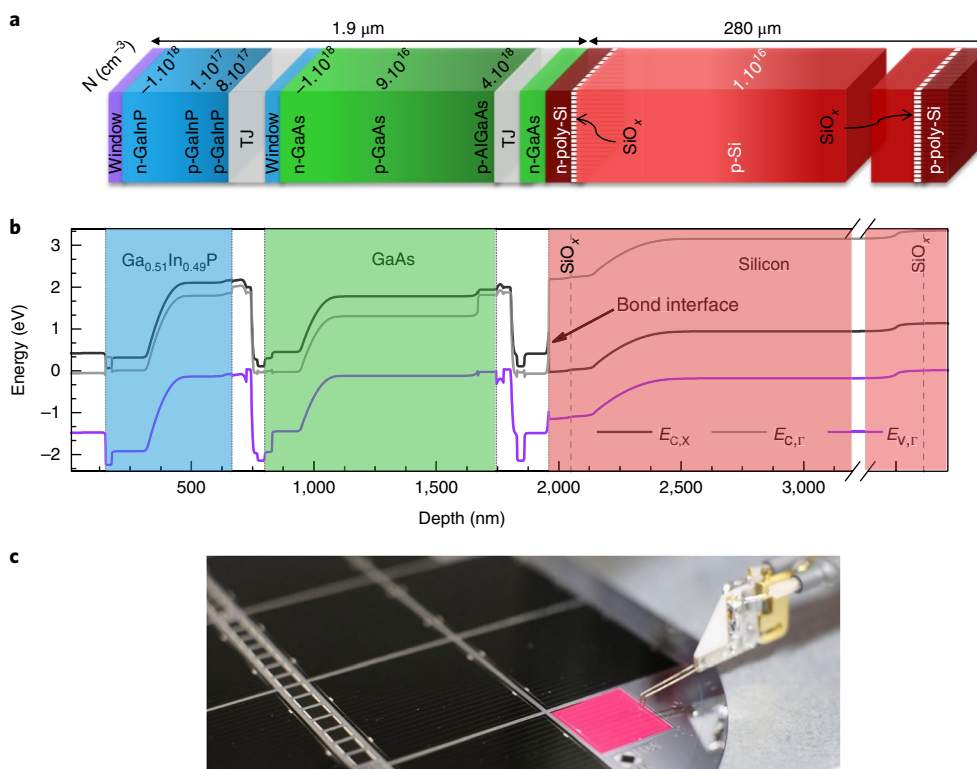


**Fig. 1 | Structure of the two-terminal wafer-bonded III-V//Si triple-junction cell. a**, Layer stack (not to scale) of the  $\text{Ga}_{0.51}\text{In}_{0.49}\text{P}/\text{GaAs}/\text{Si}$  solar cell. Subcells are connected by tunnel junctions (TJ) to form a series-connected two-terminal device. The light enters the device (left side) through the anti-reflection coating, and passes the AllnP window before reaching the 490-nm-thick first  $\text{Ga}_{0.51}\text{In}_{0.49}\text{P}$  absorber (1.90 eV direct bandgap). Photons transmitted through the top cell are absorbed in the 880-nm-thick GaAs cell beneath (bandgap 1.43 eV) and those transmitted also through the middle cell reach the silicon bottom solar cells (bandgap 1.12 eV). **b**, The semiconductor band structure is shown under an open-circuit condition without illumination for the valence band  $E_{V,\Gamma}$  (purple line) and the two lowest conduction bands at the  $\Gamma$  (direct transition, grey line) and X (indirect transition, black line) symmetry points of the crystal ( $E_{C,\Gamma}$  and  $E_{C,X}$  respectively). The  $\text{Ga}_{0.51}\text{In}_{0.49}\text{P}$ , GaAs and Si materials are represented by the blue, green and red areas respectively, while the white areas in-between represent tunnel-junction materials. The vertical dashed lines in the silicon area represent ultrathin  $\text{SiO}_x$  layers. **c**, Photograph of  $\text{Ga}_{0.51}\text{In}_{0.49}\text{P}/\text{GaAs}/\text{Si}$  triple-junction solar cells (4 cm<sup>2</sup> and 1 cm<sup>2</sup>) on a 4-inch wafer. A forward bias applied on the contacted cell results in emission of red light ( $\approx 650$  nm) from the  $\text{Ga}_{0.51}\text{In}_{0.49}\text{P}$  top cell.

A structured front side leads to an oblique light incidence inside the silicon wafer that increases the path length and the probability for total internal reflections in the wafer. However, structuring the front side is not compatible with the bonding process or with direct growth. Integrating random pyramids on the rear side of a silicon solar cell offers efficient light trapping<sup>42</sup>; however, passivation of such textured surfaces with p-type poly-Si, as applied at the back side of our device, remains challenging<sup>43</sup>. Moreover, inverted pyramids and the corresponding passivation/contact structure may degrade during the direct wafer bonding, which requires several kilonewtons of pressure. Furthermore, the rear texturing and contacting increases the complexity of the overall process flow. Solutions for alternative light-trapping concepts based on near-field effects, resonances and waveguide modes, which are more relevant for planar and/or thin absorbers, are discussed in the literature<sup>14,44</sup>. In fact, it is possible to combine electrically flat interfaces with optically structured rear-side designs, to benefit from both high voltage (low effective surface recombination) and high current. For wafer-based silicon solar cells, the effectiveness of this approach was proven with planar single-junction cells having optimized rear-side diffraction gratings<sup>45–47</sup>. As shown in Fig. 4a, we have developed an optically structured back side beneath the p<sup>+</sup> passivating contact: it features a diffractive crossed grating made of a polymeric resist, covered with silver that is evaporated on top. We used the nanoimprint lithography technique<sup>34,35,48</sup> to pattern the diffractive structure at the rear side of our III–V//Si tandem

device (details in Methods). The cross-section scanning electron microscope (SEM) image of such a poly-Si/resist/silver back side is displayed in Fig. 4b, as well as a SEM tilted view of the grating before metal evaporation (Fig. 4c). The implemented grating goes beyond the state of the art in various respects: the grating consists of a low-refractive-index epoxy material. Due to the etching step for the removal of the resist residual layer, the epoxy surface features a stochastic nanostructure that introduces additional scattering. The silver layer itself is modulated and therefore plays a strong active role in the light trapping. Finally, this photonic light-trapping structure acts at the same time as the electrical contact, thus forming a metallic photonic contact layer. The picture of the full wafer back side (Fig. 4d) illuminated with white light confirms the diffractive behaviour of this new back side. This beneficial effect is also confirmed at the cell level (see Fig. 4e). The reflectivity beyond 1,000 nm strongly decreases after applying the nanoimprinted grating, reducing the escape loss from light not absorbed in the device by 2.1 mA cm<sup>-2</sup>. This enhanced absorption leads to a 1.1 mA cm<sup>-2</sup> increase of the photocurrent in the silicon cell as extracted from the EQE. The current increase is lower than the gain in absorption. This is attributed to parasitic absorption for example at the interface between the rear-side resist and the metal, which turns out to be slightly roughened on the nanometre scale. The additional current generated by the silicon bottom cell directly improves the triple-junction cell as the silicon subcell was limiting the overall current flow in the series-connected device.

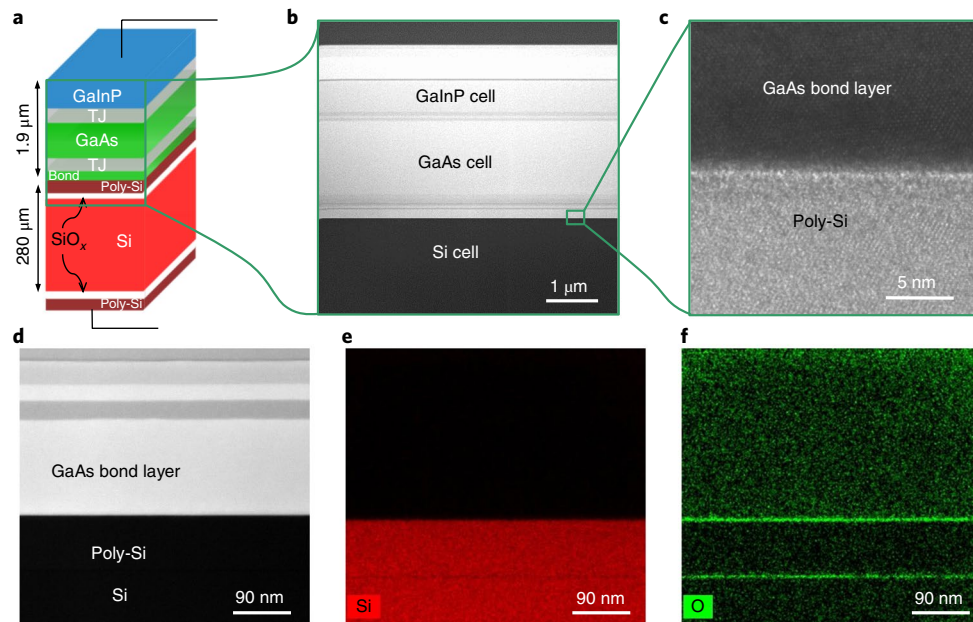


**Fig. 2 | Characteristics of the III-V//Si wafer-bonded interface.** **a**, Schematic of the monolithic wafer-bonded III-V//Si cell. From top to bottom: GaInP (blue), tunnel junction (TJ; grey), GaAs (green), TJ (grey), bond layer (green), poly-Si (dark red), SiO<sub>x</sub> (white dash), Si wafer (red) and SiO<sub>x</sub>/poly-Si layer back contact. **b**, A cross-section STEM-HAADF image of the GaInP/GaAs top cells and the upper part of the Si bottom cell. **c**, High-resolution transmission electron microscope zoom of the GaAs//poly-Si bond interface. **d**, STEM-HAADF zoom of the GaAs//poly-Si/Si interface. **e,f**, STEM-EDXS silicon map (red colour for Si) (**e**), and oxygen map (green colour for O) (**f**) of the same cross-section area.

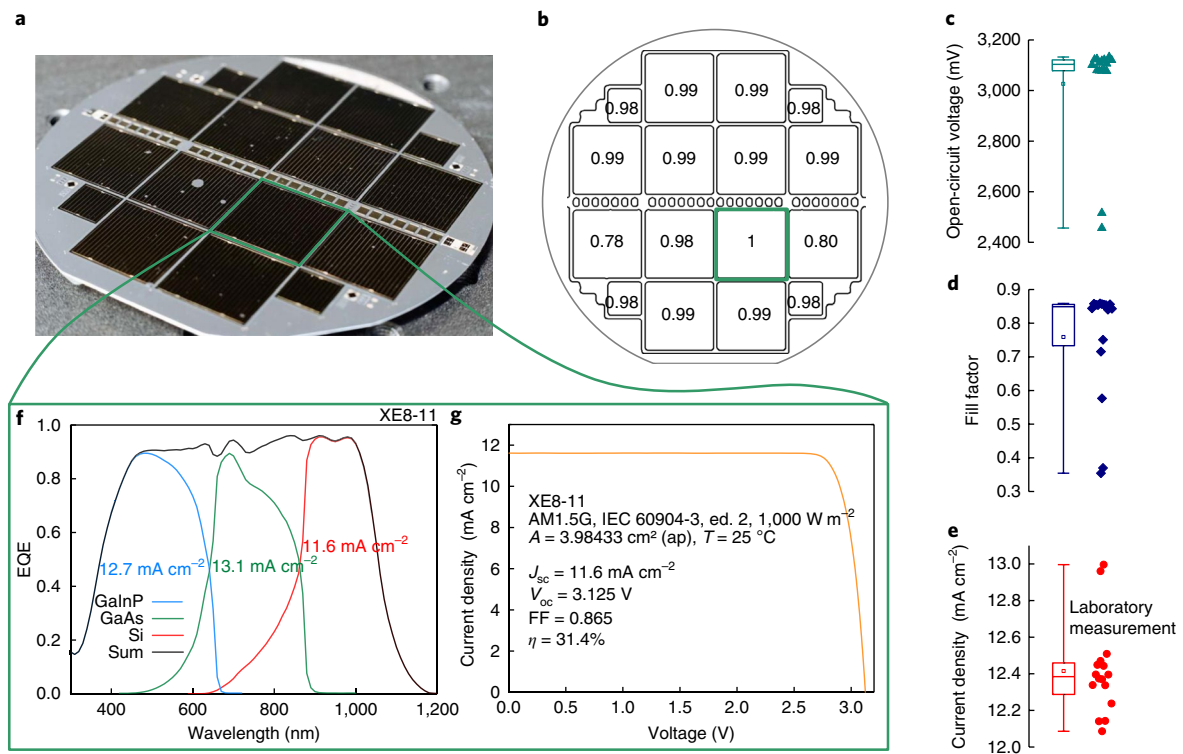


**Fig. 3 | Performance and statistics of GaInP/GaAs//Si cells without light trapping.** **a**, A photo of the 4-inch solar cell wafer with twelve 4 cm<sup>2</sup> cells and four 1 cm<sup>2</sup> cells. **b**, Voltage map of the 16 cells after normalization with the best cell voltage 3.125 V. **c–e**, Box plots (minimum–maximum, 25–75%, mean: open square symbol, median: solid line) showing the statistical distributions of the parameters of the 16 solar cells measured without shading mask (laboratory measurement). **f**, EQE of the three subcells as well as the sum of the EQEs, measured at Fraunhofer ISE CaLab. **g**, *I*–*V* characteristics measured using a spectrally adjustable solar simulator in the Fraunhofer ISE CaLab, with an aperture (*A*) of 3.984 cm<sup>2</sup>; the spectrum was adjusted to match the photo-generated current density of each subcell under AM1.5G.  $\eta$ , efficiency.

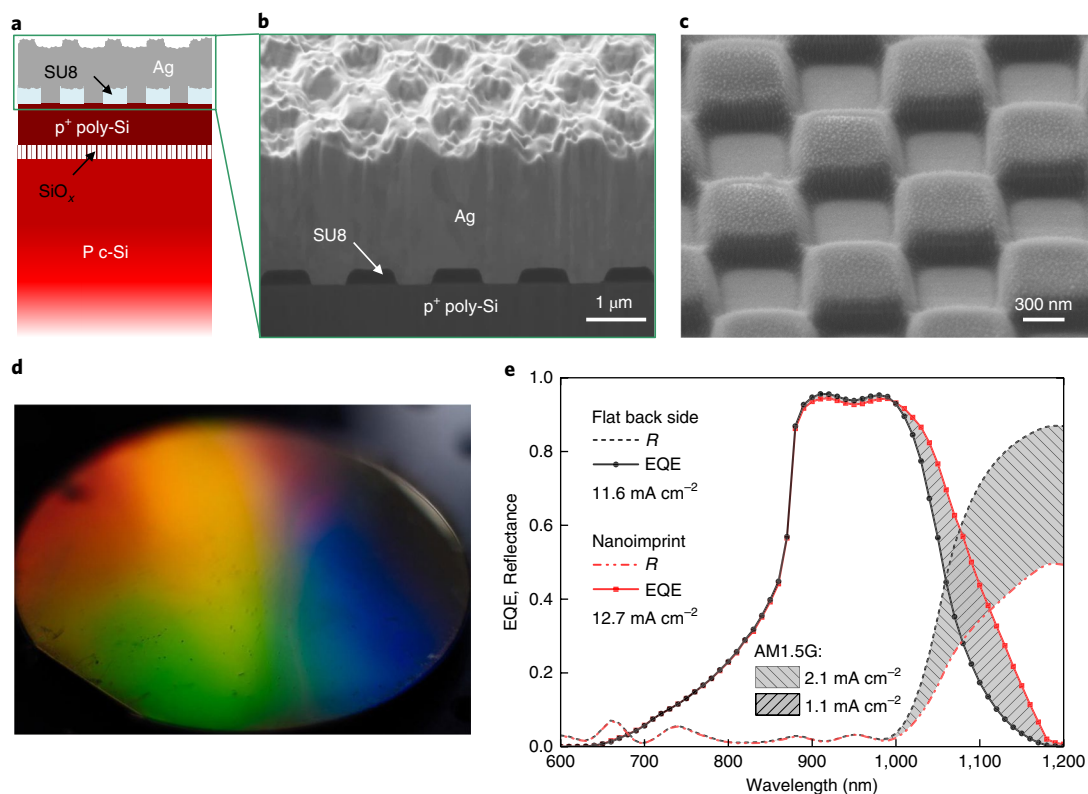


**Fig. 4 | Enhancing the infrared response of silicon with a photonic light-trapping structure.** **a**, A schematic of the electrically flat (poly-Si back side contact) but optically structured Si back side, with a nanoimprinted diffraction grating. **b**, A cross-section SEM image of the Si solar cell with a passivated contact and a nanoimprint grating (SU8 resist) covered by evaporated metal (Ag). **c**, A tilted SEM view of the nanoimprinted SU8 resist grating before metal evaporation. **d**, A photograph of the 4-inch GaInP/GaAs/Si triple-junction solar cell back side with nanoimprinted grating diffracting the incident light. **e**, A comparison of the triple-junction solar cell reflectance ( $R$ ) and silicon subcell EQE for the same cell before (see Fig. 3f) and after implementing the back-side nanoimprint grating.

### III-V//Si harvesting one-third of the AM1.5G energy

The planar III-V//Si solar cell wafer shown in Fig. 3 was re-processed to replace the flat back-side silver contact by the above-mentioned diffraction grating. The near-bandgap boost in the silicon bottom cell brings the best device close to current matching:  $12.6 \text{ mA cm}^{-2}$ ,  $12.9 \text{ mA cm}^{-2}$  and  $12.7 \text{ mA cm}^{-2}$  (from top to bottom) as calculated from EQE measurements (Fig. 5a). Escape losses (area

above  $1-R$  in Fig. 5a) sum up to  $3.8 \text{ mA cm}^{-2}$ , and additional losses of  $4.7 \text{ mA cm}^{-2}$  result from recombination and parasitic absorption (see the hatched area in Fig. 5a). The calibrated efficiency of the best solar cell with a back-side grating reaches 33.3%, as shown in Fig. 5b, owing to enhanced light trapping in the silicon bottom solar cell, which brings the device close to current matching. The voltage remains unchanged (within measurement uncertainties) and the FF

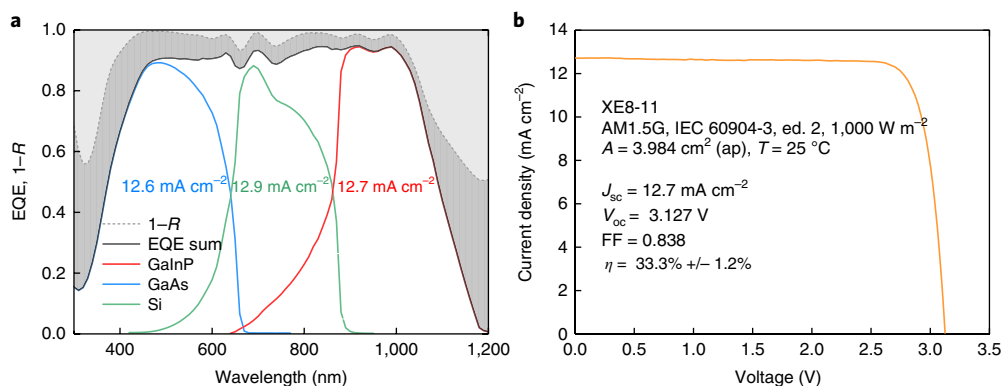


**Fig. 5 | Performance of the best two-terminal III-V//Si cell with passivating contacts and a photonic light-trapping structure.** **a**, EQE of the three subcells as well as their sum and  $1-R$ . Escape losses (grey area above  $1-R$ ) sum up to  $3.8 \text{ mA cm}^{-2}$ , and recombination and parasitic absorption result in  $4.7 \text{ mA cm}^{-2}$  losses (hatched grey area). **b**,  $I-V$  characteristics measured under a spectrally adjustable solar simulator in the Fraunhofer ISE CalLab, under an aperture of  $3.984 \text{ cm}^2$  (see Methods for uncertainties); the spectrum was adjusted to match the photo-generated current density of each subcell under AM1.5G.

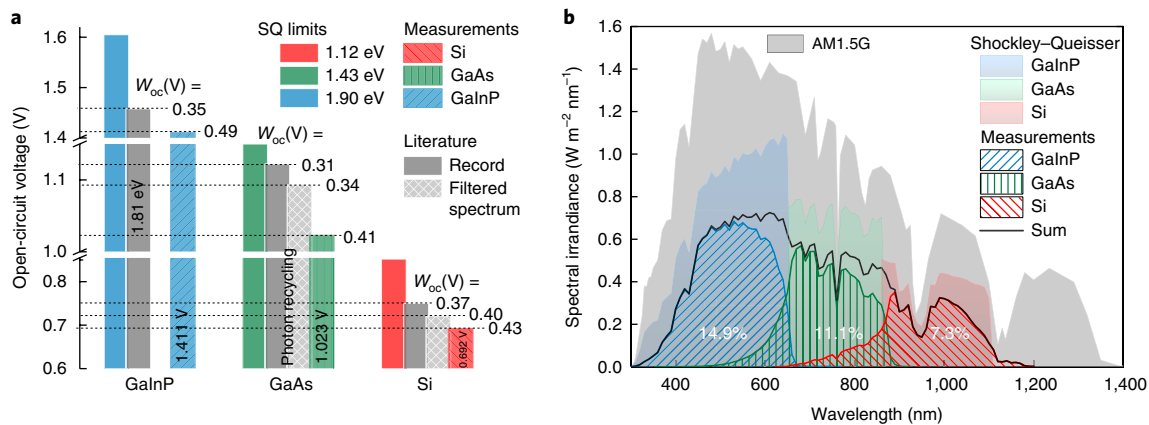


**Fig. 6 | Benchmarking of two-terminal III-V//Si cell subcell  $V_{oc}$  and spectrum utilization plot. a**, Benchmark of our subcells' open-circuit voltages ( $V_{oc}$ ) with the theoretical Shockley-Queisser (SQ) limit, literature values<sup>10</sup> under 1 sun ( $1,000 \text{ W m}^{-2}$ ) and the filtered spectrum by the corresponding upper cells ( $333 \text{ W m}^{-2}$ ). **b**, Utilization of the 1-sun AM1.5G spectrum by GaInP/GaAs//Si individual subcells in our device. The filled and dashed areas indicate, respectively, the theoretical (Shockley-Queisser) and measured contributions (using EQE, EL,  $V_{oc}$  and FF) of each subcell, and the black line refers to their sum. The absolute efficiency contribution by each subcell to the triple-junction device is: 14.9% Ga<sub>0.51</sub>In<sub>0.49</sub>P, 11.1% GaAs and 7.3% Si.

decreases slightly due to the better current matching and a small shunt that has been introduced during the rework of the rear-side contact. The low shunt resistance of the current-limiting GaInP cell allows a higher current to flow at  $J_{sc}$  where the GaInP cell is in reverse bias. This explains the difference between the measured current of  $12.7 \text{ mA cm}^{-2}$  at zero volts compared to  $12.6 \text{ mA cm}^{-2}$  calculated from the EQE of the current-limiting top cell.

The subcell voltages, 1.412 V, 1.027 V and 0.689 V (see Methods and Supplementary Figs. 2 and 3), are benchmarked against the theoretical Shockley-Queisser limit as well as literature values<sup>10</sup> in Fig. 6a. While just assuming the Shockley-Queisser limit is not sufficient, the comparison with best-in-class single-junction voltages is more relevant, especially when the spectrum filtering from the top cells is taken into account (see Supplementary Table I). Using the bandgap-voltage offset  $W_{oc}$  figure of merit<sup>49</sup>, our silicon bottom cell generates a voltage that is only 30 mV lower than the best reported silicon cell after spectrum filtering ( $W_{oc} \sim 400 \text{ mV}$ )<sup>50</sup>. The GaAs cell with a  $W_{oc}$  of 400 mV and the GaInP cell with a  $W_{oc}$  of 490 mV leave further room for improvements. This underlines the need for better top-cell material quality.

Finally, we evaluate the contribution of each subcell to the power conversion efficiency, using the product  $J_{sc}(\lambda) \times V_{oc} \times \text{FF}$ , where  $J_{sc}$  is extracted from the EQE measurements, FF is the measured value from the two-terminal triple-junction  $I$ - $V$  characteristics and  $V_{oc}$  corresponds to the calculated subcell voltage (see Methods). This calculation leads to the hashed areas in Fig. 6b. The diagram reveals significant losses compared to the idealized Shockley-Queisser (coloured areas), which arise from non-radiative recombination and partial transparency of the absorber materials. The total extracted power (that is, the sum of the three individual curves) corresponds to the black line. Note that the spectrum utilization by the silicon cell beyond 1,107 nm is explained by the indirect transitions allowing sub-bandgap absorption. From top to bottom, the absolute efficiency contribution to the triple-junction cell device is: 14.9% Ga<sub>0.51</sub>In<sub>0.49</sub>P, 11.1% GaAs and 7.3% Si, respectively.

## Conclusion

In conclusion, we have fabricated monolithic two-terminal III-V//Si triple-junction wafer-bonded solar cells featuring an innovative silicon bottom-cell design. Highly doped poly-Si/SiO<sub>x</sub> passivating and carrier-selective contacts were used on both sides of a monocrystalline p-Si wafer. This design was shown to be compatible with wafer bonding and III-V tandem solar cell processing, with

the passivation quality remaining un-altered throughout the fabrication process. A silicon subcell open-circuit voltage >690 mV was achieved under the AM1.5G spectrum filtered by GaInP/GaAs top cells. In addition, we have fabricated a back-side diffraction grating, with a nanoimprint technique, which results in an electrically flat but optically structured rear side and strongly enhances the internal light trapping. This leads to a short-circuit current density gain of  $1.1 \text{ mA cm}^{-2}$  due to near-bandgap absorption enhancement. Our best two-terminal III-V//Si cell, with a silicon bottom cell featuring passivating, carrier-selective contacts and a back-side diffraction grating, converts 33.3% of the AM1.5G photon energy into electricity. This is a significant improvement beyond the state of art for two-terminal silicon-based solar cells. The path towards higher performances will be continued by implementing higher-bandgap top cells and material quality improvements for the GaInP cell. Then, efficiencies in the range of 35% should be realistically achievable with a wafer-bonded III-V//Si two-terminal device. Finding a way to scale up this approach and bring the cost down remains an important challenge.

## Methods

**III-V solar cell epitaxial growth.** An inverted Ga<sub>0.51</sub>In<sub>0.49</sub>P (GaInP hereafter)/GaAs dual-junction solar cell structure was grown by metal-organic vapour phase epitaxy onto a (100) GaAs substrate with 6° offcut towards <111>B. The reactor was an Aix2800-G4-TM with an 8 × 100 mm substrate configuration. The growth was based on arsine, phosphine, trimethylgallium, trimethylindium and trimethylaluminium, diluted in hydrogen carrier gas. The pressure during growth was 50 mbar and process temperatures varied between 500 and 700 °C, and V/III ratios between 2 and 142. The layer structure starts with a GaAs buffer followed by an n-GaInP etch stop layer and an n-GaAs cap layer that is introduced to form ohmic contacts to the front surface of the solar cell. This layer is selectively removed between the metal grid fingers during device processing. The next layer is an n-AlInP window (indirect bandgap of 2.3 eV) that serves as the front surface field of the top cell. The Ga<sub>0.51</sub>In<sub>0.49</sub>P cell has a p-AlGaInP back surface field followed by a first p<sup>+</sup>-AlGaAs/n<sup>+</sup>-GaInP tunnel diode that changes the polarity from p-type to n-type and allows the series connection with the GaAs middle cell. The middle cell uses n-GaInP as the front-surface field and p-AlGaAs as the back-surface field and is followed by a second tunnel diode that is composed of p<sup>+</sup>-AlGaAs and n<sup>+</sup>-GaAs. The last layer of the inverted top tandem structure is a n-GaAs bond layer with a high doping level of  $10^{19} \text{ cm}^{-3}$ . Chemical mechanical polishing of the last layer was performed at the company III/V Reclaim and resulted in a r.m.s. roughness of <0.5 nm. Such a low surface roughness is a requirement for achieving good bond quality.

**Silicon solar cell fabrication.** Double-side polished p-type FZ c-Si wafers (4 Ω cm, 280 μm) were used for the silicon bottom cell. To form the poly-Si/SiO<sub>x</sub> carrier-selective contacts<sup>33</sup>, the wafers were dipped in hydrofluoric acid (HF)

followed by immersion in boiling nitric acid (69 wt%, 110 °C), thereby growing a thin tunnel oxide layer. Intrinsic a-Si was then deposited on both sides, in a LPCVD reactor. Thereafter, the n-, respectively p-, contact layer was formed by phosphorus (P), respectively boron-monofluoride (BF), implantation at low energy. Finally, subsequent to a cleaning step, the wafers underwent an annealing step in a tube furnace at 850 °C (N<sub>2</sub>), to activate the implanted species, to remove damage introduced during the implantation step and to recrystallize the a-Si layer. To further improve the surface passivation, the samples were subjected to a remote plasma hydrogen passivation process at 400 °C for 30 min. The following doping levels were measured in poly-Si layers:  $N_{D,poly} \sim 1.5 \times 10^{20} \text{ cm}^{-3}$  and  $N_{A,poly} \sim 3 \times 10^{19} \text{ cm}^{-3}$ . Before wafer bonding, the front n-type poly-Si received chemical mechanical polishing to achieve a low surface particle contamination and r.m.s. roughness; the chemical mechanical polishing step removed ~20 nm of the poly-Si layer thickness, and the resulting r.m.s. roughness was <0.5 nm.

**Surface-activated wafer bonding.** Direct semiconductor bonding of the GaInP/GaAs tandem structure to the Si bottom cell was performed at the company EVG in Austria using the EVG580 ComBond cluster tool. The process included the transfer of the wafers into a high-vacuum ambient (~10<sup>-8</sup> mbar), the removal of oxides and hydrocarbons by ComBond surface activation (ion-beam process) and the room-temperature bonding of the samples under a mechanical pressure of 2.5 kN. A post-bonding annealing step at 290 °C was performed to enhance bond strength between GaAs and silicon. The bonded wafer pairs revealed low void densities and high bond strengths that were compatible with further cell processing.

**III–V//Si solar cell processing.** The GaAs growth substrate was subsequently etched away using a solution of NH<sub>3</sub>/H<sub>2</sub>O<sub>2</sub> that selectively stops on the first GaInP layer. The GaInP etch stop was then removed in HCl, giving access to the n-GaAs cap layer. Front-side processing followed a sequence of GaAs cap removal between the grid fingers, evaporation and lift-off of a 65 nm Ta<sub>2</sub>O<sub>5</sub>/110 nm MgF<sub>2</sub> double-layer anti-reflection coating, evaporation and lift-off of a metal sequence of Pd/Au/Ge/Ti/Pd/Ag with a total thickness of 2,200 nm for the front contact. The contact was annealed at 290 °C for 1 min and the process continued by mesa etching of the cell structure with a depth of ~6 μm into the silicon wafer to separate adjacent solar cell devices. As a result, on one 4-inch wafer, twelve solar cells with an area of 4.028 cm<sup>2</sup> and four cells with area of 1.014 cm<sup>2</sup> were defined. The big cells (respectively, small cells) have 4 contact pads (2, respectively) and 5-μm-wide fingers, resulting in nominal ~0.8% (1.1%) front-side shading. As a last step, silver was evaporated on the Si back side after a short HF-dip.

**Rear-side light trapping.** To implement back-side light trapping, the Ag back-side metal contact was mechanically removed, after solar cell characterizations. In the successive step, a photonic metal structure was realized via nanoimprint lithography (NIL). The master structure, from which the polydimethylsiloxane (PDMS) stamp for NIL was replicated, was realized using interference lithography<sup>51</sup>. SU8 photoresist<sup>52</sup> was directly spin-coated on the back-side poly-Si, and thermally assisted roller-ultraviolet-NIL was used to transfer the pattern (square pads, pitch 1 μm, depth 350 nm, FF 50%) from the PDMS stamp to the SU8 (refs 34,35,48). A reactive-ion etching oxygen/argon plasma step was performed to remove any SU8 photoresist residuals between the pads that additionally implements a scattering nanostructure on top of the grating. This was followed by an HF-dip and Ag evaporation, thus ensuring a good ohmic contact at the poly-Si/Ag interface between the SU8 photoresist pads.

**III–V//Si device characterization.** Detailed structural and chemical composition of the III–V//Si wafer bonded interface region was studied by transmission electron microscopy at Fraunhofer IMWS. The experiments were conducted on a cross-section lamella prepared by a standard FIB procedure and ex situ lift out. TEM/STEM studies were performed using a TITAN<sup>3</sup> G2 80–300 microscope with an X-FEG electron gun at 300 keV, featuring a spherical-aberration corrector, a superX EDXS analyser and a STEM-HAADF detector.

The screening of all solar cell performances on the wafer was performed with a class A solar simulator from Oriel Corporation equipped with a xenon lamp. The most promising cells were then characterized in the Fraunhofer ISE calibration laboratory. External quantum efficiencies (EQEs) were measured using a grating monochromator set-up with adjustable bias voltage and bias spectrum<sup>53,54</sup>. Reflection measurements were performed on an integrated LOANA measurement device. One-sun *I*–*V* characteristics were measured under a spectrally adjustable sun simulator with one xenon lamp and two halogen lamp fields that are adjusted in intensity independently of each other to generate exactly the same current densities in each subcell as under illumination with the AM1.5G spectrum (IEC 90604-3, ed. 2 with 1,000 W m<sup>-2</sup>). The spectral correction procedure was based on a linear equation system and is equivalent to a generalized mismatch correction procedure<sup>55</sup>. The cell temperature was held at 25 °C during the measurement. An aperture mask with an area of 3.984 cm<sup>2</sup> was placed on top of the III–V//Si solar cell to avoid any contribution of photo-generated carriers from outside the defined cell area. The solar cell results were therefore referred to as aperture area measurements, which include shading by the busbars and metal fingers on the

front surface of the III–V//Si solar cell. An electroluminescence (EL) spectrum was measured by applying a bias voltage to the III–V//Si solar cell and measuring both the resulting forward current density and the emission spectrum between 600 and 1,400 nm. Three distinct peaks were observed at 1.90 eV for the disordered GaInP top cell, 1.43 eV for the GaAs middle cell and 1.09 eV for the bottom Si cell. The last value is below the indirect bandgap of silicon of 1.12 eV and correlates with the extended absorption seen in EQE measurements. The spectral EL together with the EQE and the overall open-circuit voltage of the monolithic device were used to separate the voltage contribution of each of the individual subcells following the procedure published in earlier studies<sup>56–58</sup>. This led to the  $V_{oc,meas}$  values for each of the junctions in Fig. 6a and Supplementary Table 1. The error bar on the efficiency number of the best device is the result of uncertainty analysis taking into account different elements, such as uncertainty of the reference cell, non-uniformity of the illumination of the sun simulator, uncertainty in the measurement of the spectral distribution of the sun simulator, uncertainty in the device area and EQE, adjustment for thickness difference between the reference cell and the device under test, adjustment of temperature and so on.

**Data availability.** The data that support the plots within this paper and other findings of this study are available from the corresponding author upon reasonable request.

Received: 29 October 2017; Accepted: 27 February 2018;

Published online: 02 April 2018

## References

- Green, M. A. The path to 25% silicon solar cell efficiency: History of silicon cell evolution. *Prog. Photovolt. Res. Appl.* **17**, 183–189 (2009).
- Masuko, K. et al. Achievement of more than 25% conversion efficiency with crystalline silicon heterojunction solar cell. *IEEE J. Photovolt.* **4**, 1433–1435 (2014).
- Smith, D. D. et al. Toward the practical limits of silicon solar cells. *IEEE J. Photovolt.* **4**, 1465–1469 (2014).
- Glunz, S. W. et al. The irresistible charm of a simple current flow pattern – 25% with a solar cell featuring a full-area back contact. In *Proc. 31st European Photovoltaic Solar Energy Conference and Exhibition* 259–263 (2015); <https://doi.org/10.4229/EUPVSEC20152015-2BP.1.1>
- Adachi, D., Hernández, J. L. & Yamamoto, K. Impact of carrier recombination on fill factor for large area heterojunction crystalline silicon solar cell with 25.1% efficiency. *Appl. Phys. Lett.* **107**, 233506 (2015).
- Polman, A., Knight, M., Garnett, E. C., Ehrler, B. & Sinke, W. C. Photovoltaic materials: Present efficiencies and future challenges. *Science* **352**, aad4424 (2016).
- Battaglia, C., Cuevas, A. & Wolf, S. D. High-efficiency crystalline silicon solar cells: status and perspectives. *Energy Environ. Sci.* **9**, 1552–1576 (2016).
- Richter, A. et al. n-Type Si solar cells with passivating electron contact: identifying sources for efficiency limitations by wafer thickness and resistivity variation. *Sol. Energy Mater. Sol. Cells* **173**, 96–105 (2017).
- Yoshikawa, K. et al. Silicon heterojunction solar cell with interdigitated back contacts for a photoconversion efficiency over 26%. *Nat. Energy* **2**, 17032 (2017).
- Green, M. A. et al. Solar cell efficiency tables (version 50). *Prog. Photovolt. Res. Appl.* **25**, 668–676 (2017).
- Shockley, W. & Queisser, H. J. Detailed balance limit of efficiency of p–n junction solar cells. *J. Appl. Phys.* **32**, 510 (1961).
- Richter, A., Hermle, M. & Glunz, S. W. Reassessment of the limiting efficiency for crystalline silicon solar cells. *IEEE J. Photovolt.* **3**, 1184–1191 (2013).
- Mitchell, B. et al. Four-junction spectral beam-splitting photovoltaic receiver with high optical efficiency. *Prog. Photovolt. Res. Appl.* **19**, 61–72 (2011).
- Polman, A. & Atwater, H. A. Photonic design principles for ultrahigh-efficiency photovoltaics. *Nat. Mater.* **11**, 174–177 (2012).
- Goldschmidt, J. C., Do, C., Peters, M. & Goetzberger, A. Spectral splitting module geometry that utilizes light trapping. *Sol. Energy Mater. Sol. Cells* **108**, 57–64 (2013).
- Green, M. A. et al. 40% efficient sunlight to electricity conversion. *Prog. Photovolt. Res. Appl.* **23**, 685–691 (2015).
- Sheng, X. et al. Printing-based assembly of quadruple-junction four-terminal microscale solar cells and their use in high-efficiency modules. *Nat. Mater.* **13**, 593–598 (2014).
- Mathews, I. et al. Adhesive bonding for mechanically stacked solar cells. *Prog. Photovolt. Res. Appl.* **23**, 1080–1090 (2015).
- Essig, S. et al. Raising the one-sun conversion efficiency of III–V//Si solar cells to 32.8% for two junctions and 35.9% for three junctions. *Nat. Energy* **2**, 17144 (2017).
- Albrecht, S. & Rech, B. Perovskite solar cells: On top of commercial photovoltaics. *Nat. Energy* **2**, 16196 (2017).

21. Bush, K. A. et al. 23.6%-efficient monolithic perovskite/silicon tandem solar cells with improved stability. *Nat. Energy* **2**, 17009 (2017).
22. Werner, J., Niesen, B. & Ballif, C. Perovskite/silicon tandem solar cells: marriage of convenience or true love story? – An overview. *Adv. Mater. Interfaces* **5**, 1700731 (2018).
23. Essig, S. et al. Wafer-bonded GaInP/GaAs/Si solar cells with 30% efficiency under concentrated sunlight. *IEEE J. Photovolt.* **5**, 977–981 (2015).
24. Baba, M. et al. Feasibility study of two-terminal tandem solar cells integrated with smart stack, areal current matching, and low concentration. *Prog. Photovolt. Res. Appl.* **25**, 255–263 (2017).
25. Lee, K.-H. et al. Assessing material qualities and efficiency limits of III–V on silicon solar cells using external radiative efficiency. *Prog. Photovolt. Res. Appl.* **24**, 1310–1318 (2016).
26. Cariou, R. et al. Monolithic two-terminal III–V/Si triple-junction solar cells with 30.2% efficiency under 1-sun AM1.5g. *IEEE J. Photovolt.* **7**, 367–373 (2017).
27. Yu, Z. J., Leilaoui, M. & Holman, Z. Selecting tandem partners for silicon solar cells. *Nat. Energy* **1**, 16137 (2016).
28. Bolkhovityanov, Y. B. & Pchelyakov, O. P. GaAs epitaxy on Si substrates: modern status of research and engineering. *Phys. Usp.* **51**, 437 (2008).
29. Umeno, M., Kato, T., Egawa, T., Soga, T. & Jimbo, T. High efficiency AlGaAs/Si tandem solar cell over 20%. *Sol. Energy Mater. Sol. Cells* **41–42**, 395–403 (1996).
30. Grassman, T. J., Chmielewski, D. J., Carnevale, S. D., Carlin, J. A. & Ringel, S. A. GaAs<sub>0.7</sub>P<sub>0.23</sub>/Si dual-junction solar cells grown by MBE and MOCVD. *IEEE J. Photovolt.* **6**, 326–331 (2016).
31. Ohlmann, J. et al. Influence of metal-organic vapor phase epitaxy reactor environment on the silicon bulk lifetime. *IEEE J. Photovolt.* **6**, 1668–1672 (2016).
32. Feldmann, F., Bivour, M., Reichel, C., Hermle, M. & Glunz, S. W. Passivated rear contacts for high-efficiency n-type Si solar cells providing high interface passivation quality and excellent transport characteristics. *Sol. Energy Mater. Sol. Cells* **120**, 270–274 (2014).
33. Feldmann, F., Reichel, C., Müller, R. & Hermle, M. The application of poly-Si/SiO<sub>x</sub> contacts as passivated top/rear contacts in Si solar cells. *Sol. Energy Mater. Sol. Cells* **159**, 265–271 (2017).
34. Hauser, H. et al. Honeycomb texturing of silicon via nanoimprint lithography for solar cell applications. *IEEE J. Photovolt.* **2**, 114–122 (2012).
35. Tucher, N., Höhn, O., Hauser, H., Müller, C. & Bläsi, B. Characterizing the degradation of PDMS stamps in nanoimprint lithography. *Microelectron. Eng.* **180**, 40–44 (2017).
36. Yablonovitch, E., Gmitter, T., Swanson, R. M. & Kwarq, Y. H. A 720 mV open circuit voltage SiO<sub>x</sub>:c-Si:SiO<sub>x</sub> double heterostructure solar cell. *Appl. Phys. Lett.* **47**, 1211–1213 (1985).
37. Gan, J. Y. & Swanson, R. M. Polysilicon emitters for silicon concentrator solar cells. In *Proc. IEEE Conference on Photovoltaic Specialists* Vol. 1, 245–250 (1990); <https://doi.org/10.1109/PVSC.1990.111625>
38. Yan, D., Cuevas, A., Bullock, J., Wan, Y. & Samundsett, C. Phosphorus-diffused polysilicon contacts for solar cells. *Sol. Energy Mater. Sol. Cells* **142**, 75–82 (2015).
39. Peibst, R. et al. Working principle of carrier selective poly-Si/c-Si junctions: Is tunnelling the whole story? *Sol. Energy Mater. Sol. Cells* **158**, 60–67 (2016).
40. Flotgen, C., Razek, N., Dragoi, V. & Wimplinger, M. Novel surface preparation methods for covalent and conductive bonded interfaces fabrication. *ECS Trans.* **64**, 103–110 (2014).
41. Häussler, D. et al. Aberration-corrected transmission electron microscopy analyses of GaAs/Si interfaces in wafer-bonded multi-junction solar cells. *Ultramicroscopy* **134**, 55–61 (2013).
42. Campbell, P. & Green, M. A. Light trapping properties of pyramidally textured surfaces. *J. Appl. Phys.* **62**, 243–249 (1987).
43. Larionova, Y. et al. On the recombination behavior of p<sup>+</sup>-type polysilicon on oxide junctions deposited by different methods on textured and planar surfaces: On the recombination behavior of p<sup>+</sup>-type polysilicon on oxide junctions. *Phys. Status Solidi A* **214**, 1700058 (2017).
44. Atwater, H. A. & Polman, A. Plasmonics for improved photovoltaic devices. *Nat. Mater.* **9**, 205–213 (2010).
45. Peters, M., Rüdiger, M., Hauser, H., Hermle, M. & Bläsi, B. Diffractive gratings for crystalline silicon solar cells—optimum parameters and loss mechanisms. *Prog. Photovolt. Res. Appl.* **20**, 862–873 (2012).
46. Eisenlohr, J. et al. Rear side sphere gratings for improved light trapping in crystalline silicon single junction and silicon-based tandem solar cells. *Sol. Energy Mater. Sol. Cells* **142**, 60–65 (2015).
47. Eisenlohr, J. et al. Efficiency increase of crystalline silicon solar cells with nanoimprinted rear side gratings for enhanced light trapping. *Sol. Energy Mater. Sol. Cells* **155**, 288–293 (2016).
48. Hauser, H. et al. Development of nanoimprint processes for photovoltaic applications. *J. Micro/Nanolithogr. MEMS MOEMS* **14**, 031210 (2015).
49. King, R. R. et al. Band gap-voltage offset and energy production in next-generation multijunction solar cells. *Prog. Photovolt. Res. Appl.* **19**, 797–812 (2011).
50. Taguchi, M. et al. 24.7% record efficiency HIT solar cell on thin silicon wafer. *IEEE J. Photovolt.* **4**, 96–99 (2014).
51. Wolf, A. J. et al. Origination of nano- and microstructures on large areas by interference lithography. *Microelectron. Eng.* **98**, 293–296 (2012).
52. Shaw, J. M., Gelorme, J. D., LaBianca, N. C., Conley, W. E. & Holmes, S. J. Negative photoresists for optical lithography. *IBM J. Res. Dev.* **41**, 81–94 (1997).
53. Meusel, M. et al. Spectral response measurements of monolithic GaInP/Ga(In)As/Ge triple-junction solar cells: measurement artifacts and their explanation. *Prog. Photovolt. Res. Appl.* **11**, 499–514 (2003).
54. Siefer, G., Gandy, T., Schachtner, M., Wekkeli, A. & Bett, A. W. Improved grating monochromator set-up for EQE measurements of multi-junction solar cells. In *Proc. 2013 IEEE 39th Photovoltaic Specialists Conference (PVSC)* 0086–0089 (2013); <https://doi.org/10.1109/PVSC.2013.6744105>
55. Meusel, M., Adelhelm, R., Dimroth, F., Bett, A. W. & Warta, W. Spectral mismatch correction and spectrometric characterization of monolithic III–V multi-junction solar cells. *Prog. Photovolt. Res. Appl.* **10**, 243–255 (2002).
56. Rau, U. Reciprocity relation between photovoltaic quantum efficiency and electroluminescent emission of solar cells. *Phys. Rev. B* **76**, 085303 (2007).
57. Roensch, S., Hoheisel, R., Dimroth, F. & Bett, A. W. Subcell I–V characteristic analysis of GaInP/GaInAs/Ge solar cells using electroluminescence measurements. *Appl. Phys. Lett.* **98**, 251113 (2011).
58. Kirchartz, T. et al. Internal voltages in GaInP/GaInAs/Ge multijunction solar cells determined by electroluminescence measurements. *Appl. Phys. Lett.* **92**, 123502 (2008).

## Acknowledgements

The authors thank the Fraunhofer ISE employees E. Oliva, A. Schütte, R. Koch, M. Graf, E. Schäffer, M. Schachtner, E. Fehrenbacher, A. Wekkeli, K. Wagner, S. Stättner, R. Freitas, A. Lösel, A. Leimenstoll, F. Schätzle and V. Klinger for helping with device processing and characterization. We also thank T. Höche and C. Patzig from Fraunhofer IMWS for the TEM studies. We further acknowledge financial support through the European Union's Horizon 2020 research and innovation programme under the Marie Skłodowska-Curie HISTORIC grant agreement no. 655272 and the German Ministry for Economic Affairs and Energy through the project PoTaSi (no. 0324247). The development of the Si bottom cell received funding through the EU project NanoTandem under grant agreement no. 641023. This article reflects only the authors' view and the funding agency is not responsible for any use that may be made of the information it contains.

## Author contributions

R.C. carried out experiments in the laboratory, theoretical modelling and evaluation of the data; R.C. and J.B. led the process development and optimization. F.F., M.H. and S.W.G. developed the passivating and carrier-selective contact Si bottom cell; S.W.G. also performed the analysis of spectrum utilization in Fig. 5d. P.B. improved the III–V layer structure and performed the epitaxy growth. D.L. performed band structure simulations and coordinated the epitaxy research. N.R. performed the wafer bonding and coordinated the TEM analysis; M.W. supervised the wafer bonding collaboration and led the design of the EVG580 ComBond cluster tool. O.H. and H.H. proposed the idea of the specific rear-side diffraction grating and developed and fabricated the crossed grating together. B.B. supported the understanding and fine-tuning of the rear-side grating and coordinated the photonic light-trapping research. G.S. supervised the cell calibration and ensured the accuracy of the measurements. A.W.B. supported discussions and editing of the manuscript and F.D. developed the concept of two-terminal III–V/Si tandem cells by direct wafer bonding and contributed to many aspects of the cell design and process optimization. All co-authors participated in the discussions and improvements of this manuscript.

## Competing interests

The authors N. Razek and M. Wimplinger are employed by EV Group E. Thallner GmbH, 4782 St Florian am Inn, Austria, which produces the wafer bonding machine used in this study.

## Additional information

**Supplementary information** is available for this paper at <https://doi.org/10.1038/s41560-018-0125-0>.

**Reprints and permissions information** is available at [www.nature.com/reprints](http://www.nature.com/reprints).

**Correspondence and requests for materials** should be addressed to R.C.

**Publisher's note:** Springer Nature remains neutral with regard to jurisdictional claims in published maps and institutional affiliations.

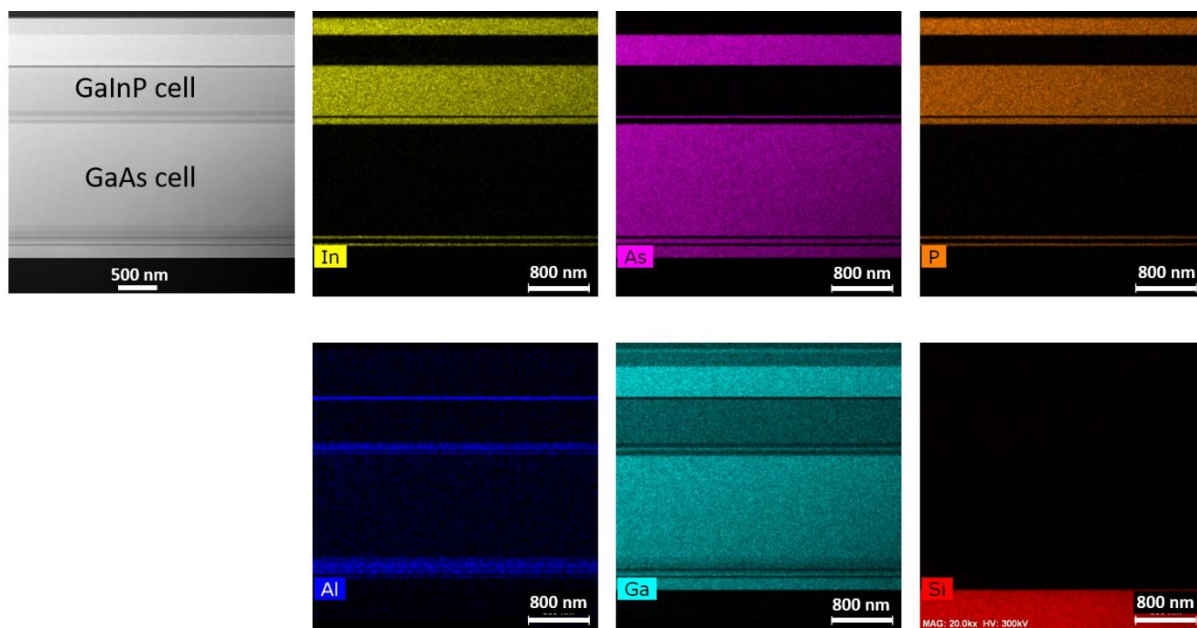
In the format provided by the authors and unedited.

# III-V-on-silicon solar cells reaching 33% photoconversion efficiency in two-terminal configuration

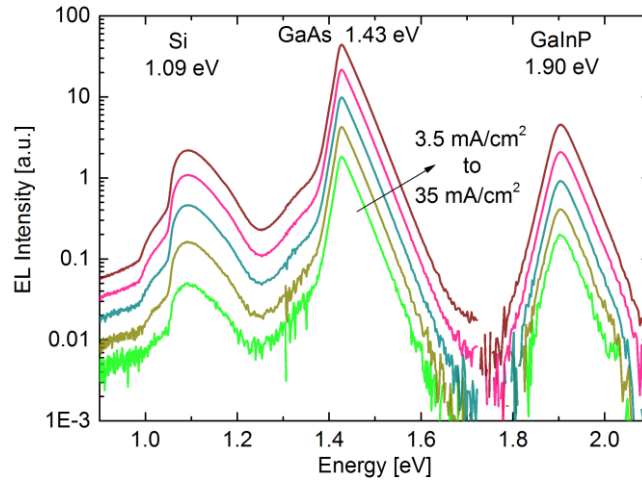
Romain Cariou <sup>1,4\*</sup>, Jan Benick<sup>1</sup>, Frank Feldmann<sup>1,2</sup>, Oliver Höhn<sup>1</sup>, Hubert Hauser<sup>1</sup>, Paul Beutel<sup>1</sup>, Nasser Razek<sup>3</sup>, Markus Wimplinger<sup>3</sup>, Benedikt Bläsi<sup>1</sup>, David Lackner<sup>1</sup>, Martin Hermle<sup>1</sup>, Gerald Siefer<sup>1</sup>, Stefan W. Glunz<sup>1,2</sup>, Andreas W. Bett<sup>1</sup> and Frank Dimroth <sup>1</sup>

---

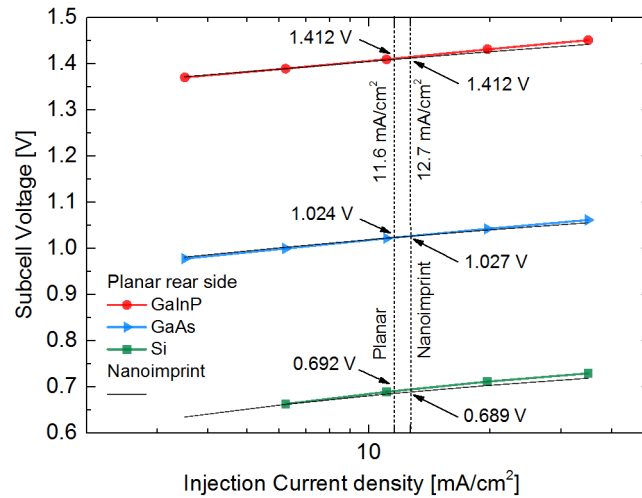
<sup>1</sup>Fraunhofer Institute for Solar Energy Systems ISE, Freiburg, Germany. <sup>2</sup>Laboratory for Photovoltaic Energy Conversion, University of Freiburg, Freiburg, Germany. <sup>3</sup>EV Group E. Thallner GmbH, St Florian am Inn, Austria. <sup>4</sup>Present address: Université Grenoble Alpes, CEA, LITEN, INES, Grenoble, France.  
\*e-mail: [romain.cariou@cea.fr](mailto:romain.cariou@cea.fr)



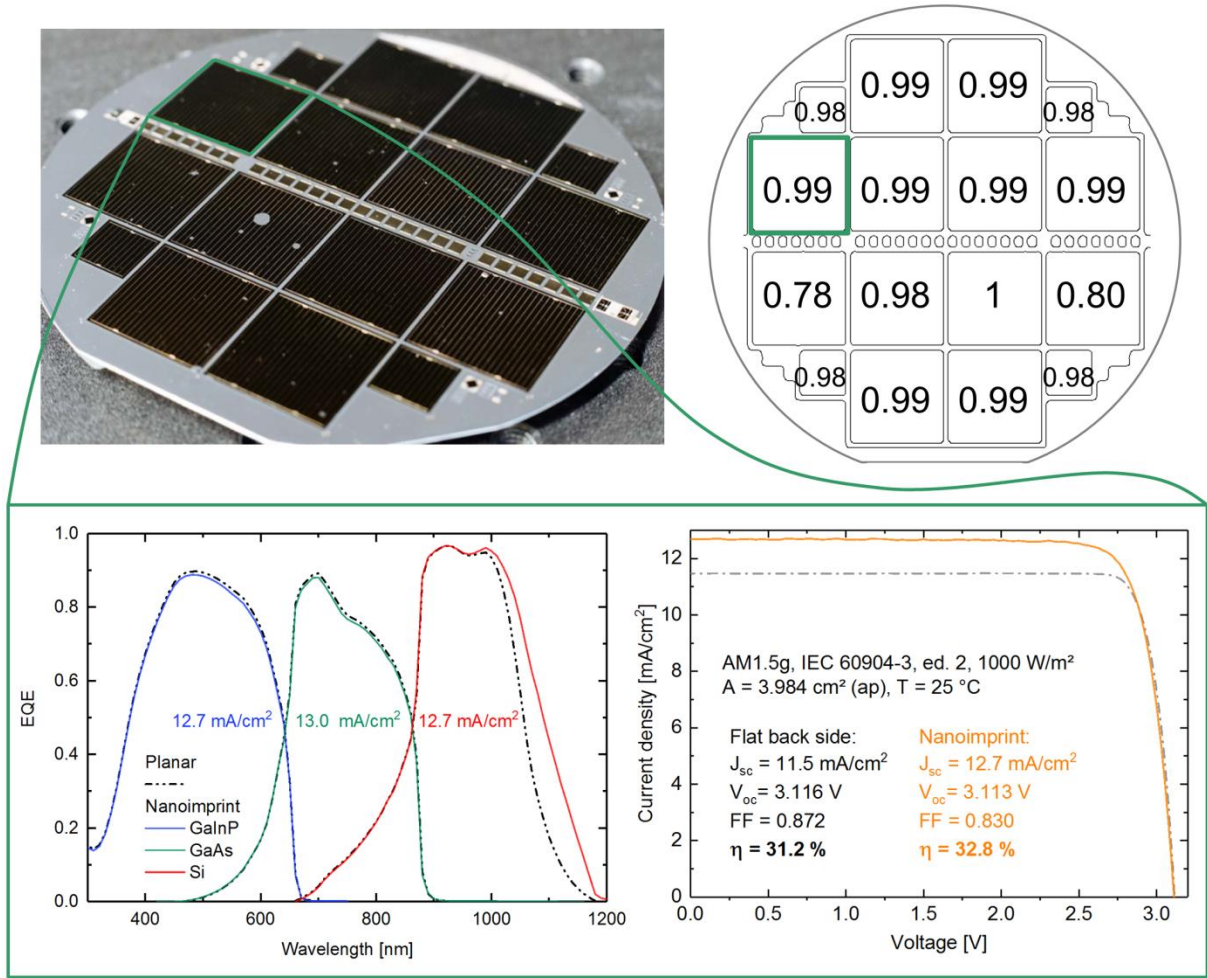
**Supplementary Figure 1: STEM-HAADF and STEM-EDXS maps of In, As, P, Al, Ga and Si elements measured for a GaInP/GaAs/Si solar cell cross section. The various layers (absorber, barriers, tunnel junctions, etc.) can be clearly distinguished.**



**Supplementary Figure 2: Electroluminescence spectrum of the record GaInP/GaAs/Si solar cell at current densities between 3.5 and 35 mA/cm<sup>2</sup> (from green to dark red curve).** One can clearly see the emission of each junction at 1.9 eV for the GaInP top cell, at 1.43 eV for the GaAs middle cell and at 1.09 eV for the Si bottom cell. The bottom cell electroluminescence is significantly suppressed due to the indirect nature of the semiconductor.



**Supplementary Figure 3: Subcell open-circuit voltages for the GaInP/GaAs/Si triple-junction cell.** Result are extracted from the electroluminescence in combination with the external quantum efficiency and calibrated with the overall voltage of the triple-junction cell at 1-sun AM1.5g. This leads to the individual subcell voltages as a function of current density. Circles, triangles and squares correspond to GaInP, GaAs and Si (with planar rear side) subcell voltages, respectively. Dark lines correspond to subcell voltages for the same solar cell, but with additional diffraction grating on the silicon rear side.



**Supplementary Figure 4: Calibrated measurements of the 2<sup>nd</sup> best GaInP/GaAs//Si cell on the 4-inch wafer.** Top left – picture of the solar cell 4-inch wafer. Top right –  $V_{oc}$  distribution among the 16 cells (2x2 cm<sup>2</sup> & 1x1 cm<sup>2</sup>), normalized to the record cell voltage (3.125V). Bottom left – subcell EQE of the triple-junction cell before (dash line) and after adding Si rear side diffraction grating. Bottom right - IV-characteristics measured under a spectrally adjustable solar simulator in the Fraunhofer ISE CalLab, with an aperture of 3.984 cm<sup>2</sup>, before (dash line) and after adding a Si rear side diffraction grating. The spectrum is adjusted to match the photo-generated current density of each subcell under AM1.5g.

**Supplementary Table 1: Benchmark of GaInP, GaAs & Si subcell parameters achieved in this study against theoretical and experimental values from literature.**  $V_{oc,SQ}$  and  $FF_{SQ}$  refer to the subcell voltage in the radiative limit after Shockley and Queisser,  $V_{oc,Auger,filtr.}$  to the Auger limit under the filtered spectrum,  $V_{oc, lit.}$  and  $V_{oc, lit. filtr.}$  to literature record cells under 1-sun and filtered spectrum.  $V_{oc, meas}$  corresponds to the experimental voltage values in this study, extracted from EQE and EL measurements. The values in the grey (resp. white) boxes in this table are under 1/3-sun (resp. 1-sun) AM1.5g spectrum. In triple-junction configuration, the GaAs middle and Si bottom subcells have necessarily a lower performance than single-junction devices under the full AM1.5g spectrum, since they receive only the light “filtered” by the upper subcell(s).  $V_{oc, filtr.}$  is calculated as follow:  $V_{oc, filtr.} = V_{oc} + kT/q \times \ln(1/3)$ , with  $kT/q$  being the thermal voltage (26mV at room temperature).

Subcell material	Bandgap [eV]	$FF_{SQ}$ [%]	$V_{oc,SQ}$ [V]	$V_{oc, lit.}$ [V]	$V_{oc,Auger,filtr.}$ [V]	$V_{oc, lit. filtr.}$ [V]	$V_{oc, meas}$ [V]
GaInP	1.90	91.8	1.605	1.458 ( $E_g=1.81\text{eV}$ )	-	-	1.412
GaAs	1.43	89.5	1.150	1.122	-	1.093	1.027
Si	1.12	86.6	0.852	0.75	0.741	0.721	0.689